Langmuir
Article
pubs.acs.org/Langmuir

Formation of Green Rust Sulfate: A Combined in Situ Time-Resolved X-ray Scattering and Electrochemical Study

Imad A. M. Ahmed,*,† Liane G. Benning,† Gabriella Kakonyi,† Aryani D. Sumoondur,† Nick J. Terrill,‡ and Samuel Shaw†

†School of Earth & Environment, University of Leeds, U.K., and ‡Diamond Light Source, Didcot, Oxford, U.K.

Received October 16, 2009. Revised Manuscript Received February 11, 2010

The mechanism of green rust sulfate (GR-SO_4) formation was determined using a novel in situ approach combining time-resolved synchrotron-based wide-angle X-ray scattering (WAXS) with highly controlled chemical synthesis and electrochemical (i.e., *Eh* and pH) monitoring of the reaction. Using this approach,GR-SO_4 was synthesized under strictly anaerobic conditions by coprecipitation from solutions with known Fe^{II}/Fe^{III} ratios (i.e., 1.28 and 2) via the controlled increase of pH. The reaction in both systems proceeded via a three-stage precipitation and transformation reaction. During the first stage,schwertmannite ($Fe_8O_8(OH)_{4.5}(SO_4)_{1.75}$) precipitated directly from solution at pH 2.8−4.5. With increasing pH (>5), Fe^{2+} ions adsorb to the surface of schwertmannite and catalyze its transformation to goethite (α-FeOOH) during the second stage of the reaction. In the third stage, the hydrolysis of the adsorbed Fe^{2+} ions on goethite initiates its transformation to GR-SO_4 at pH >7. The GR-SO_4 then continues to crystallize up to pH ∼8.5. These results suggest that with an Fe^{II}/Fe^{III} ratio of ≤2 in the initial solution the structural Fe^{II}/Fe^{III} of the GR-SO_4 will be close to that of the starting composition.

1. Introduction

Green rust (GR) compounds are a unique class of layered double-hydroxide (LDH) phases with the general formula $[Fe^{II}_{(1-x)}Fe^{III}_x(OH)_2]^{x+}\cdot[(x/n)A^{n-})\cdot mH_2O]^{x-}$[1,2] where $x = Fe^{III}/Fe_{total}$, A^{n-} denotes interlayer anions whose charge is n, and m is moles of water molecules. The GR crystal structure consists of positively charged brucite-like layers of edge-sharing octahedrally coordinated Fe^{II} and Fe^{III} hydroxide units intercalated with anionic species and water molecules.[3] The most studied GR phases are those with Fe^{II}/Fe^{III} ratios equal to 2 and 3, but a number of studies have indicated a range of Fe^{II}/Fe^{III} ratios from ≥1 to 3.0.[4−8] A recent study by Christiansen et al.[9] reported that the interlayer of green rust sulfate (GR-SO_4) also contains Na^+ ions, leading to an ideal formula of $NaFe^{II}_6Fe^{III}_3(OH)_{18}(SO_4)_2\cdot 12H_2O$, although the Fe/OH ratio is the same in sodium and sodium-free GR structures. Various types of anions can be intercalated into the GR structure, including organic (e.g., lactate and formate)[10−12] and inorganic species[13] (e.g., SO_4^{2-}, CO_3^{2-}, and Cl^-).[14,15] Sulfate-containing GR structures are among the most studied forms and have been found to occur in a number of engineered and geoenvironmental systems.[13,16−18] For example, GR-SO_4 was shown to form as part of corrosion products on steel exposed to sulfate-rich seawater[16−18] and at oxic−anoxic interfaces in hydromorphic soils.[19,20]

*Corresponding author. Current address: The University of Lancaster, Lancaster Environment Centre, Lancaster, U.K. LA1 4YQ. Phone: +44(0)1524510211. E-mail: i.ahmed@lancaster.ac.uk.

(1) Refait, P.; Géhin, A.; Abdelmoula, M.; Genin, J. M. R. Coprecipitation thermodynamics of iron(II-III) hydroxysulphate green rust from Fe(II) and Fe(III) salts. *Corros. Sci.* **2003**, *45*, 659−676.

(2) Ruby, C.; Aissa, R.; Géhin, A.; Cortot, J.; Abdelmoula, M.; Génin, J. M. R. Green Rusts synthesis by coprecipitation of Fe^{II}-Fe^{III} ions and mass-balance diagram. *C. R. Geosci.* **2006**, *338*, 420−432.

(3) Simon, L.; Francois, M.; Refait, P.; Renaudin, G.; Lelaurain, M.; Génin, J. M. R. Structure of the Fe(II-III) layered double hydroxysulphate Green Rust two from Rietveld analysis. *Solid State Sci.* **2003**, *5*, 327−334.

(4) Cuttler, A. H.; Man, V.; Cranshaw, T. E.; Longworth, G. A Moessbauer study of green rust precipitates; I, Preparations from sulphate solutions. *Clay Miner.* **1990**, *25*, 289−301.

(5) Kukkadapu, R. K.; Zachara, J. M.; Fredrickson, J. K.; Kennedy, D. W. Biotransformation of two-line silica-ferrihydrite by a dissimilatory Fe(III)-reducing bacterium: formation of carbonate Green Rust in the presence of phosphate. *Geochim. Cosmochim. Acta* **2004**, *68*, 2799−2814.

(6) Legrand, L.; Abdelmoula, M.; Géhin, A.; Chaussé, A.; Génin, J. M. R. Electrochemical formation of a new Fe(II)---Fe(III) hydroxy-carbonate green rust: characterisation and morphology. *Electrochim. Acta* **2001**, *46*, 1815−1822.

(7) Ona-Nguema, G.; Abdelmoula, M.; Jorand, F.; Benali, O.; Géhin, A.; Block, J. C.; Genin, J. M. R. Iron (II, III) hydroxycarbonate Green Rust formation and stabilization from lepidocrocite bioreduction. *Environ. Sci. Technol.* **2002**, *36*, 16−20.

(8) Ruby, C.; Géhin, A.; Aissa, R.; Ghanbaja, J.; Abdelmoula, M.; Génin, J. M. R. Chemical stability of hydroxysulphate green rust synthetised in the presence of foreign anions: carbonate, phosphate and silicate. *Hyperfine Interact.* **2006**, *167*, 803−807.

(9) Christiansen, B. C.; Balic-Zunic, T.; Petit, P. O.; Frandsen, C.; Mørup, S.; Geckeis, H.; Katerinopoulou, A.; Stipp, S. L. S. Composition and structure of an iron-bearing, layered double hydroxide (LDH) - Green rust sodium sulphate. *Geochim. Cosmochim. Acta* **2009**, *73*, 3579−3592.

(10) Sabot, R.; Jeannin, M.; Gadouleau, M.; Guo, Q.; Sicre, E.; Refait, P. Influence of lactate ions on the formation of rust. *Corros. Sci.* **2007**, *49*, 1610−1624.

(11) Refait, P.; Abdelmoula, M.; Genin, J. M. R.; Jeannin, M. Synthesis and characterisation of the Fe(II-III) hydroxy-formate green rust. *Hyperfine Interact.* **2006**, *167*, 717−722.

(12) Sumoondur, A. D.; Shaw, S.; Benning, L. G. Formation of lactate intercalated Green Rust *via* the reductive dissolution of ferrihydrite. *Geochim. Cosmochim. Acta* **2009**, *73*, A1291.

(13) Génin, J. M. R.; Ruby, C. Anion and cation distributions in Fe(II-III) hydroxysalt Green Rusts from XRD and Mössbauer analysis (carbonate, chloride, sulphate, ...); the "Fougerite" mineral. *Solid State Sci.* **2004**, *6*, 705−718.

(14) Drissi, S. H.; Refait, P.; Abdelmoula, M.; Génin, J. M. R. The preparation and thermodynamic properties of Fe(II)-Fe(III) hydroxide-carbonate (Green Rust 1): Pourbaix diagram of iron in carbonate-containing aqueous media. *Corros. Sci.* **1995**, *37*, 2025−2041.

(15) Refait, P.; Génin, J. M. R. The oxidation of ferrous hydroxide in chloride-containing aqueous media and pourbaix diagrams of green rust one. *Corros. Sci.* **1993**, *34*, 797−819.

(16) Olowe, A. A.; Genin, J. M. R. The mechanism of oxidation of ferrous hydroxide in sulphated aqueous media: Importance of the initial ratio of the reactants. *Corros. Sci.* **1991**, *32*, 965−984.

(17) Refait, P.; Abdelmoula, M.; Genin, J. M. R.; Sabot, R. Green rusts in electrochemical and microbially influenced corrosion of steel. *Compt. Rend. Geosciences* **2006**, *338*, 476−487.

(18) Stampfl, P. P. Ein basisches eisen-II-III-karbonat in rost. *Corros. Sci.* **1969**, *9*, 185−187.

(19) Génin, J. M. R.; Aissa, R.; Géhin, A.; Abdelmoula, M.; Benali, O.; Ernstsen, V.; Ona-Nguema, G.; Upadhyay, C.; Ruby, C. Fougerite and Fe^{II-III} hydroxycarbonate Green Rust; ordering, deprotonation and/or cation substitution; structure of hydrotalcite-like compounds and mythic ferrosic hydroxide $Fe(OH)_{(2+x)}$. *Solid State Sci.* **2005**, *7*, 545−572.

The presence of structural Fe^{II} means that GRs have the capacity to reduce a range of inorganic and organic species, including toxic metals[21−23] (e.g., CrO_4^{2-}, UO_2^{2+}, and Hg^{2+}) and organic pollutants[24] (e.g., trichloroethene (TCE)). These reduction processes can lead to the breakdown of the organic molecules (e.g., TCE) or the formation of highly insoluble reduced inorganic phases (e.g., UO_2(s)), thus reducing the environmental bioavailability of these toxic species. These unique properties have led to increasing interest in GRs as potential materials in pollution prevention and environmental waste minimization technologies such as engineered permeable reactive barrier systems (PRBs).[25] Understanding the formation and geochemical stability of GR in engineered and other environmental systems is key to assessing its potential role in the natural biogeochemical iron cycle and engineered environments (e.g., PRBs).

In the laboratory, GR compounds are commonly synthesized using either oxidation or coprecipitation techniques. The oxidation method involves progressive aerial sparging of an Fe^{II} solution (e.g., $FeSO_4$ solution) at pH 7 to 8, which leads to the partial oxidation of Fe^{II} to Fe^{III}, both of which hydrolyze to form GR.[14,16] During coprecipitation, an acidic solution containing a mixture of aqueous Fe^{2+} and Fe^{3+} cations in a sulfate or chloride medium is neutralized by the controlled addition of a basic solution.[26] Previous studies of abiotic GR-SO_4 formation via coprecipitation at different Fe^{II}/Fe^{III} ratios indicated that the first phase to form at pH ~2.5 is a ferric phase referred to as ferric hydroxysulfate basic salt,[1,27,28] which has been suggested to be schwertmannite ($Fe_8O_8(OH)_6SO_4 \cdot nH_2O$)[1,28] although this phase has not been directly identified. With a further increase in pH, this ferric phase transforms into ferric oxyhydroxide (i.e., goethite, α-FeOOH) and subsequently into GR-SO_4. Ruby et al.[28] suggested that during this latter stage the adsorption of Fe^{2+}(aq) and SO_4^{2-} ions onto the goethite surface induced its dissolution and leads to the transformation of goethite into GR-SO_4. (Free Fe^{2+} and Fe^{3+} cations and total dissolved Fe^{II} and Fe^{III} in solution are termed hereafter as Fe^{2+}(aq), Fe^{3+}(aq), Fe^{II}_{tot}(aq), and Fe^{III}_{tot}(aq), respectively.) However, the mechanisms of GR formation via these precursors have not been fully quantified.

Characterizing the formation of GR under natural and laboratory conditions is inherently difficult because of the highly air-sensitive nature of GR phases. This is primarily due to the rapid oxidation (seconds to minutes) of structural Fe^{II} in the presence of favorable electron acceptors (e.g., NO_3^- or molecular O_2). Thus, to obtain detailed information on the mechanism and kinetics of GR-SO_4 formation during coprecipitation we have developed a novel synchrotron-based method that allowed the in situ and time-resolved analysis of solid particles forming and transforming in solution, under strictly anaerobic conditions, using a controlled chemical synthesis apparatus. This system permitted the simultaneous quantification of several chemical parameters in the aqueous solutions (i.e., pH, *Eh*, moles of consumed base, and Fe^{2+}(aq) and $Fe^{3+}_{(aq)}$ concentrations) and the characterization of solid phases forming using in situ time-resolved wide angle X-ray scattering (WAXS). Using this combination of techniques, we aim to (a) demonstrate the effectiveness of the novel experimental procedure to concomitantly follow and quantify such complex aqueous and solid reactions and (b) obtain detailed information on the formation mechanism and stability of GR-SO_4 in the laboratory, which in turn provides some insight into the behavior of GR in engineered (e.g., PRBs) and natural systems (e.g., soils).

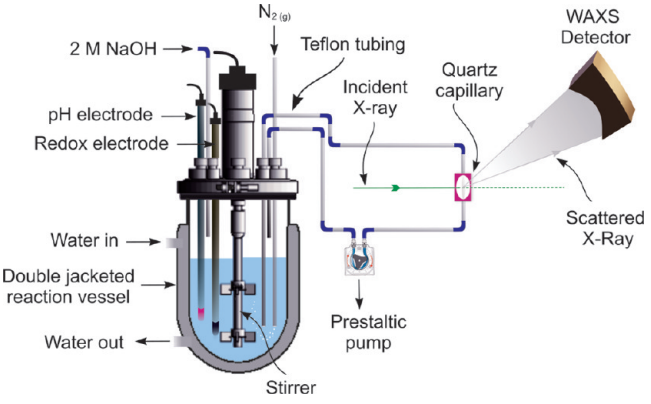

Figure 1. Schematic diagram of the experimental setup used for the synthesis of GR and the simultaneous collection of time-resolved WAXS data on stations MPW6.2 (SRS) and I22 (DLS). The reaction vessel contents were constantly circulated through a quartz capillary mounted in line with the incident X-ray beam.

2. Experimental Section

2.1. Synthesis of Green Rust. Two isothermal coprecipitation experiments were carried out to synthesize GR-SO_4 from mixed Fe^{II} (as $FeSO_4 \cdot 7H_2O$) and Fe^{III} (as $Fe_2(SO_4)_3 \cdot 6H_2O$) sulfate solutions with initial Fe^{II}/Fe^{III} ratios of 1.28:1 ($R_{1.28}$) and 2:1 ($R_{2.0}$), respectively. All solutions were prepared from oxygen-free deionized water inside a vinyl glovebox (Coy Laboratory Products Inc.) flushed with an H_2/N_2 gas mixture (5%:95%) at room temperature. The glovebox maintains a strict ≤5 ppm oxygen atmosphere through H_2(g) that reacts with a palladium catalyst to remove residual oxygen. All reagents used in this study were high-purity analytical-grade chemicals (>99% purity). Prior to the mixing of the two solutions, each individual solution was filtered through 0.2 μm cellulose nitrate membrane filters to remove possible traces of insoluble Fe^{III} solids. The starting solution consisted of a mixture of 0.2 M $FeSO_4 \cdot 7H_2O$ and 0.078 M ($R_{1.28}$) or 0.05 M ($R_{2.0}$) $Fe_2(SO_4)_3 \cdot 6H_2O$. The mixed solutions were transferred to an oxygen-free reactor (Figure 1, Infors, Switzerland) consisting of a double-jacketed glass reaction vessel fitted with an overhead stirrer, a NIST-calibrated pH electrode, a redox probe, ports for the addition of acid or base solution, a gas inflow port (for N_2(g)), an exit gas tube with a water-cooled condenser, and two ports for the inflow and outflow of the solution through a closed circulation loop (Figure 1). With this setup the pH, redox potential (*Eh*), and rate of base addition were recorded continuously via an automated control unit. During the titration experiments, the headspaces of the reaction vessel as well as that of the bottle containing the base (2.0 M NaOH, degassed) were maintained at a positive pressure of N_2(g) to

(20) Trolard, F.; Génin, J. M. R.; Abdelmoula, M.; Bourrie, G.; Humbert, B.; Herbillon, A. Identification of a green rust mineral in a reductomorphic soil by Mössbauer and Raman spectroscopies. *Geochim. Cosmochim. Acta* **1997**, *61*, 1107−1111.
(21) O'Loughlin, E. J.; Kelly, S. D.; Cook, R. E.; Csencsits, R.; Kemner, K. M. Reduction of uranium(VI) by mixed iron(II)/iron(III) hydroxide (green rust): formation of UO_2 nanoparticles. *Environ. Sci. Technol.* **2003**, *37*, 721−727.
(22) Erbs, M.; Bruun Hansen, H. C.; Olsen, C. E. Reductive dechlorination of carbon tetrachloride using iron(II) iron(III) hydroxide sulfate (green rust). *Environ. Sci. Technol.* **1999**, *33*, 307−311.
(23) Williams, A. G. B.; Scherer, M. M. Kinetics of Cr(VI) reduction by carbonate green rust. *Environ. Sci. Technol.* **2001**, *35*, 3488−3494.
(24) O'Loughlin, E. J.; Burris, D. R. Reduction of halogenated ethanes by green rust. *Environ. Toxicol. Chem.* **2004**, *23*, 41−48.
(25) Wilkin, R. T.; McNeil, M. S. Laboratory evaluation of zero-valent iron to treat water impacted by acid mine drainage. *Chemosphere* **2003**, *53*, 715−725.
(26) Ruby, C.; Aïssa, R.; Géhin, A.; Cortot, J.; Abdelmoula, M.; Génin, J. M. Green rusts synthesis by coprecipitation of Fe^{II}-Fe^{III} ions and mass-balance diagram. *C. R. Geosci.* **2006**, *338*, 420−432.
(27) Géhin, A.; Ruby, C.; Abdelmoula, M.; Benali, O.; Ghanbaja, J.; Refait, P.; Génin, J. M. R. Synthesis of Fe(II-III) hydroxysulphate green rust by coprecipitation. *Solid State Sci.* **2002**, *4*, 61−66.
(28) Ruby, C.; Géhin, A.; Abdelmoula, M.; Génin, J. M. R.; Jolivet, J. P. Coprecipitation of Fe(II) and Fe(III) cations in sulphated aqueous medium and formation of hydroxysulphate Green Rust. *Solid State Sci.* **2003**, *5*, 1055−1062.

maintain anaerobicity. The reaction cell temperature was controlled at 21 ± 1 °C by circulating constant-temperature water through the cell jacket.

GR-SO_4 was synthesized via the stepwise base titration of the mixed Fe^{II}/Fe^{III} sulfate starting solutions. This was achieved by the computer-controlled addition of a degassed (carbonate- and O_2-free) 2.0 M NaOH solution to the reaction vessel. The base was added using a highly accurate peristaltic pump (±0.05 mL) to deliver small volumes of the degassed NaOH solution. The initial mixed iron solutions had a pH of ~1.8, and this was increased to pH 7.0 over 2.2 h ($R_{1.28}$) or 2.9 h ($R_{2.0}$). The pH was then held at 7 for ~6 h ($R_{1.28}$) to investigate the effect of aging at this pH on the stability and growth of GR. This extended time was not necessary in later experiments, and thus the pH was then held at 7 for ~3.5 h for the $R_{2.0}$ experiment. Following this time at pH 7, the pH was increased to 10 over ~5 h in both the $R_{1.28}$ and $R_{2.0}$ systems. The volume of added base, pH, *Eh*, and reaction time were automatically recorded every 20 s.

2.2. In Situ Time-Resolved Scattering Experiments. The in situ wide angle X-ray scattering (WAXS) measurements for the $R_{1.28}$ experiment were performed at station MWP6.2 of the Synchrotron Radiation Source (SRS), Daresbury Laboratory, U.K., whereas the $R_{2.0}$ experiment was performed at beamline I22, Diamond Light Source (DLS), Oxford, U.K. The automated reactor described above was mounted on the beamline, and an analogue peristaltic pump was used to circulate the solution/suspension constantly from the reaction vessel in a closed loop of tubing connected to a cell consisting of a quartz capillary (1.5 mm i.d., 10 μm wall) that was directly aligned with the X-ray beam. The WAXS detector at station MPW6.2 is a multiwire gas detector based on the RAPID technology.[29,30] The detector on station I22 is a HOTWAXS detector[31] based on glass microstrip technology.[32] The wavelength of the incident X-ray beam was 1.0 Å during all experiments. The face of the WAXS detector was positioned 5−65° from the normal to the beam and close to the sample to reduce air scattering, enabling the collection of WAXS data at wide 2θ angles (Figure 1). A NIST silicon standard (SRM 640c) was used to calibrate the scattering angle on the WAXS detectors. Time-resolved WAXS patterns of the contents of the capillary were collected every 2 min.

2.3. Data Analysis. Experimental data were normalized using the XOTOKO software[33] to compensate for variations in the intensity of the incident beam due to the decay of the synchrotron beam current. Diffraction peaks within individual WAXS patterns were fitted using pseudo-Voigt profile functions implemented in the XFIT program.[34] This procedure was used to evaluate peak positions, areas, and the fwhm of each diffraction peak. The changes in peak areas with time were normalized to give the degree of reaction, $\alpha = I_{(t)}/I_{max}$, where $I_{(t)}$ represents the peak area at a given time and I_{max} is the maximum peak area during the reaction. Assuming that the diffraction peak shape can be described by a Gaussian function, the crystallite size can be approximated via the Scherrer equation[35]

$$D = \frac{k}{\beta_{hkl} \cos \theta} \times \frac{360}{2\pi} \quad (1)$$

where D is the crystallite size (Å), λ is the radiation wavelength (Å), k is the Scherrer constant, which is related to the *hkl* index and crystal shape,[36] β_{hkl} is the true fwhm of the X-ray peak due to crystallite size effects, and θ is the Bragg angle. The instrumental broadening was corrected for by subtracting the fwhm of the Si standard (SRM 640c) from the measured peaks.

2.4. Ex Situ Analyses. Solid and solution samples were collected during a series of complementary ex situ experiments that were conducted in an equivalent manner to the online in situ experiments described above, but with no WAXS data collection. Aliquots of all intermediate solid phases as well as end product GR-SO_4 were collected at various pH values, separated from the solutions by filtration (< 0.2 μm polycarbonate filters), washed with oxygen-free deionized water, and air dried inside an O_2-free glovebox. The dried solids collected at pH > 6.0 were coated with a thin layer of glycerol (purity > 99%)[37] prior to XRD analysis using a Philips PW1050 goniometer with a Cu K_α radiation X-ray tube (λ = 1.5418 Å) and a scan time of 2−4 h. Washed and dried solids collected at pH < 6.0 were analyzed by XRD with a scan time of 14 h. Subsets of the air-dried solids were placed on Al stubs and coated with Pt (3 nm layer), and the particles were imaged using field-emission gun scanning electron microscopy (FEG-SEM) (Leo Gemini 1530 FEG-SEM, Cambridge, U.K.) at 3.0 keV. High-resolution images were also recorded using a transmission electron microscope (TEM) (Philips CM20TEM, Oxford Instruments at 80 keV) after deposition on holey-carbon-coated copper TEM grids. Both TEM imaging and selected-area electron diffraction (SAED, Philips CM20TEM) were employed to characterize the crystal morphology and structure. Finally, the samples were analyzed using a diamond-accessorized attenuated total reflection Fourier transform infrared (ATR-FTIR) spectrometer (MicroLab, A_2 Technologies) for the IR spectral range between 4000 and 650 cm^{-1}. Throughout the experiments and at the same time steps as for the solids, solution samples were also removed from the reactor via one of the ports and immediately filtered and preserved with 6 N HCl. The concentrations of total dissolved Fe (Fe_{tot} (aq)) and $Fe^{II}{}_{tot}$ (aq) in these solutions were determined using the Ferrozine photometric method,[38,39] and $Fe^{III}{}_{tot}$ (aq) was determined by difference.

3. Results and Discussion

A three-dimensional representation of the time-resolved WAXS data recorded in situ for the $R_{1.28}$ experiment is shown in Figure 2. At low pH (< 2.8) the WAXS pattern consisted of only a large hump caused by scattering from the solution but with no diffraction peaks indicating the absence of any crystalline material. At pH > 2.8, on top of the broad hump a broad feature centered between 22 and 23° 2θ (2.5 −2.6 Å) formed (Figure 2). The 2θ position of this feature corresponds to the maximum intensity diffraction peak for schwertmannite (2.55 Å, (212)), and this feature transformed into a broad peak with time. This stage coincided with an increase in the optical density of the suspension

(29) Cernik, R. J.; Barnes, P.; Bushnell-Wye, G.; Dent, A. J.; Diakun, G. P.; Flaherty, J. V.; Greaves, G. N.; Heeley, E. L.; Helsby, W.; Jacques, S. D. M.; Kay, J.; Ryan, A.; Tang, C. C.; Terrill, N. J. The new materials processing beamline at the SRS Daresbury, MPW6. 2. *J. Synchrotron Radiat.* **2004**, *11*, 163−170.

(30) Terrill, N. J.; Bushnell-Wye, G.; Cernik, R. J.; Dent, A. J.; Diakun, G. P.; Flaherty, J. V.; Kay, J.; Tang, C.; Barnes, P.; Greaves, G. N.; Rayment, T.; Ryan, A., SRS Station MPW6.2 - a new facility for variable energy SAXS/WAXS at the Daresbury Laboratory. *Fibre Diffr. Rev.* **2003**, *11*, 20−27.

(31) Bateman, J. E.; Derbyshire, G. E.; Diakun, G.; Duxbury, D. M.; Fairclough, J. P. A.; Harvey, I.; Helsby, W. I.; Lipp, J. D.; Marsh, A. S.; Salisbury, J.; Sankar, G.; Spill, E. J.; Stephenson, R.; Terrill, N. J. The HOTWAXS detector. *Nucl. Instrum. Methods Phys. Res., Sect. A* **2007**, *580*, 1526−1535.

(32) Oed, A. Position-sensitive detector with microstrip anode for electron multiplication with gases. *Nucl. Instrum. Methods Phys. Res., Sect. A* **1988**, *263*, 351−359.

(33) Boulin, C.; Kempf, R.; Koch, M. H. J.; McLaughlin, S. M. Data appraisal, evaluation and display for synchrotron radiation experiments: Hardware and software. *Nucl. Instrum. Methods Phys. Res., Sect. A* **1986**, *249*, 399−407.

(34) Cheary, R. W.; Coelho, A., A fundamental parameters approach to X-ray line-profile fitting. *J. Appl. Crystallogr.* **1992**, *25*, 109−121.

(35) Patterson, A. L. The Scherrer formula for X-ray particle size determination. *Phys. Rev.* **1939**, *56*, 978.

(36) Langford, J. A.; Wilson, A. J. C. Scherrer after sixty years: a survey and some new results in the determination of crystallite size. *J. Appl. Crystallogr.* **1978**, *11*, 102−113.

(37) Hansen, H. C. B. Composition, stabilization, and light absorption of Fe(II)Fe(III) hydroxy-carbonate (green rust). *Clay Miner.* **1989**, *24*, 663.

(38) Stookey, L. L. Ferrozine: a new spectrophotometric reagent for iron. *Anal. Chem.* **1970**, *42*, 779−781.

(39) Viollier, E.; Inglett, P. W.; Hunter, K.; Roychoudhury, A. N.; Van Cappellen, P. The ferrozine method revisited: Fe(II)/Fe(III) determination in natural waters. *Appl. Geochem.* **2000**, *15*, 785−790.

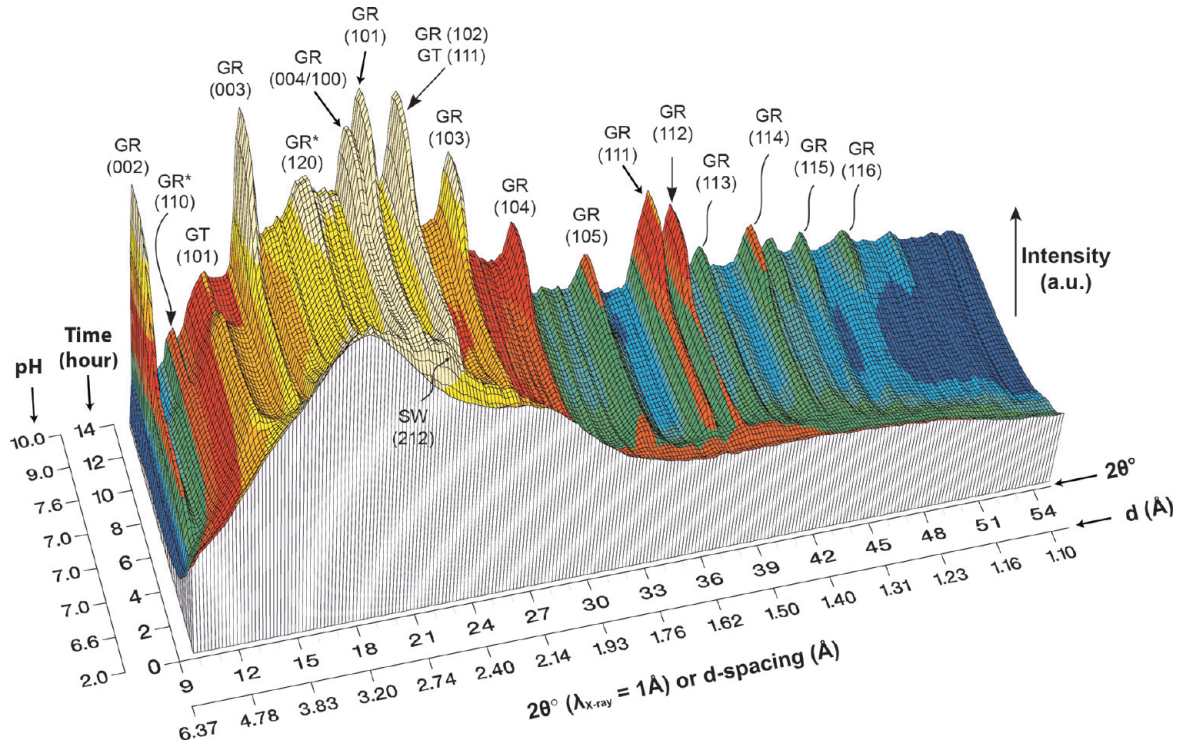

Figure 2. Three-dimensional plot of time-resolved WAXS patterns collected in situ during the $R_{1.28}$ GR-SO_4 formation experiment. The Miller indices of GR-SO_4 (GR), goethite (GT), and schwertmannite (SW) diffraction peaks are given in parentheses. Note that the incident X-ray wavelength was 1 Å. The GR peak positions match those indexed by Bernal et al.[40] and Simon et al.,[3] except for the peaks labeled GR*, which were recently indexed by Christiansen et al.[9]

above approximately pH 2.2 and a gradual change in color to orange-yellow at pH ~2.8 (Figure S1, Supporting Information). Above pH 5.0, the broad peak for schwertmannite decreased and in a second crystallization stage a peak centered at ~13.8° 2θ appeared. This peak corresponds to the maximum intensity diffraction peak for goethite (4.18 Å, (101)). Lastly, in the third stage of crystallization starting at pH ~6.8 to 7.0, several sharp diffraction peaks appear that correspond to GR-SO_4. This stage of the reaction coincided with a change in the color of the precipitate to olive green (Figure S1). The WAXS data obtained from the $R_{2.0}$ experiment (Figure S2) also shows the same three-stage reaction profile as the $R_{1.28}$ experiment (i.e., schwertmannite−goethite−GR-SO_4). As noted before, the electrochemical and titration data (i.e., *Eh*, pH, and millimoles of OH^- added) from the $R_{1.28}$ and $R_{2.0}$ experiments were recorded simultaneously with the scattering data (WAXS). Similar to the correspondence between the results from the WAXS data for both experiments, the titration data from both the $R_{1.28}$ and $R_{2.0}$ experiments (Figure S4) shows almost identical trends in OH^- consumption and equivalent trends in *Eh* and pH, with the only difference being the time spent at pH 7.0. The data from both experiments reveals that the reaction leading to the formation of GR-SO_4 follows three main stages: (i) formation of schwertmannite (pH 2.8−5.0), (ii) transformation of schwertmannite to goethite (pH 5−6.8), and (iii) formation and growth of GR-SO_4 (pH >6.8). These processes are discussed in detail in the following sections.

3.1. Schwertmannite Formation (pH 2.0−5.0). The data for the pH and base added for the first stage of the reaction ($R_{1.28}$) are shown in Figure 3a. During this stage and up to pH ~4.5, the measured pH deviated considerably from the programmed pH. This indicates that the rate of base addition was not adequate to maintain the programmed pH increase (i.e., the OH^- consumption due to hydrolysis in solution was faster than the maximum rate of base addition that the reactor-controller could supply). When pH ~2.2 was reached, orange-yellow sol-like particles were observed, resulting in an increase in the optical density of the solution (Figure S1). The analysis of Fe in solution indicates that above pH 2 the concentration of Fe^{III}_{tot} (aq) decreased rapidly and approached zero by pH ~3.5 (Figure 5), which was a consequence of the precipitation of a ferric-bearing phase (i.e., schwertmannite; see below). However, the concentration of Fe^{II}_{tot} (aq) in this pH range remained virtually unchanged. Concomitantly, a sharp drop in *Eh* from +636 to +410 mV was recorded. Because of the high concentration of Fe_{tot} (aq), the *Eh* of the solution will be controlled by the Fe^{3+}/Fe^{2+} redox couple; therefore, the increase in the Fe^{3+}/Fe^{2+} ratio in this pH range would have caused a significant decrease in *Eh*.

The formation of the colored precipitate (Figure S1, movie) and the rapid consumption of base in the system suggest that above pH ~2.0 Fe^{3+}(aq) hydrolysis and precipitation occurred (Figure 3a). In Figure 2, at pH < 5, the center of the broad WAXS peak at 22.6° 2θ (2.55 Å) was assigned to the most intense schwertmannite peak (212). This assignment was confirmed by a diffraction pattern measured ex situ from an air-dried sample collected at pH 2.8 ± 0.1 (Figure 4a) that revealed that schwertmannite was the sole phase present. Figure 5 shows a decrease in Fe^{III}_{tot}(aq) concentration at pH ~2, but schwertmannite was detected only at pH 2.8 (Figures 2 and 4). This indicates that the initially formed solid was very poorly ordered and crystallized only to a sufficient degree for detection by WAXS as the pH increased. Using the fwhm of the schwertmannite (212) peak in Figure 4a, the average crystallite size of schwertmannite particles calculated using the Scherrer equation (eq 1) was ~5 nm, which is in agreement with results obtained by Davidson et al.[41] The nanosize nature of the schwertmannite particles explains the observed broad diffraction peaks in the ex situ XRD data and the in situ WAXS data (Figures 2 and 4). The WAXS data suggest that the schwertmannite peak reaches its maximum at pH 3 to 4

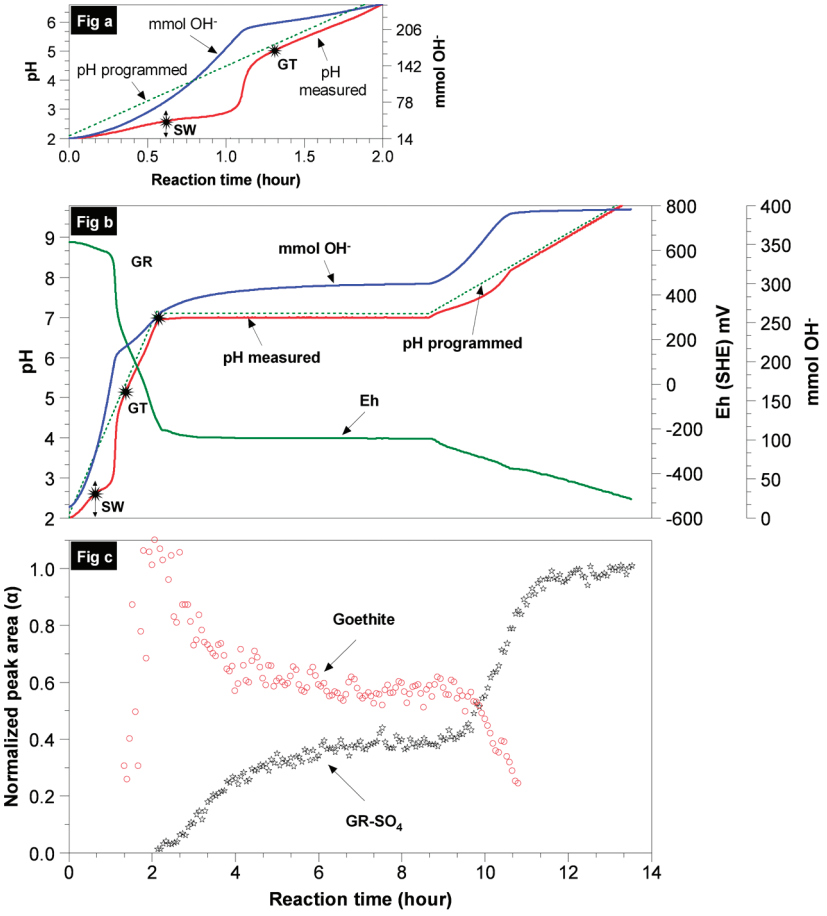

Figure 3. (a) *Eh*−pH vs time (up to 2 h) profile from the $R_{1.28}$ GR-SO_4 coprecipitation experiment. (b) *Eh*−pH vs time profile from the $R_{1.28}$ GR-SO_4 coprecipitation experiment. The time and pH at which schwertmannite, goethite, and GR-SO_4 started to form are marked with a star (*). (c) Normalized peak area vs time for the GR-SO_4 (101) and the goethite (101) diffraction peaks, with open symbols representing experimental data.

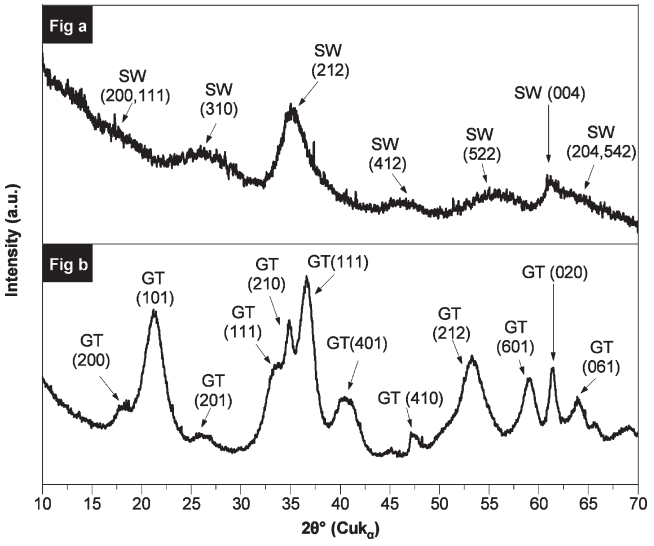

Figure 4. XRD pattern of (a) a schwertmannite sample collected at pH 2.8 and (b) goethite collected at pH 5.7 from an offline experiment carried out in an equivalent manner to the online $R_{1.28}$ experiment. The Miller indices of the goethite (GT) and schwertmannite (SW) diffraction peaks are given in parentheses.

but when the pH further increases to pH ~5.0 this broad feature begins to decline (Figure 2).

Figure 6 presents ATR-FTIR spectra of solid samples collected at different pH values during the synthesis of GR-SO_4 from an offline experiment carried out in an equivalent manner to the online $R_{2.0}$ experiment. Data from samples collected at pH 3 and 4.5 show a broad band between ~1000 and ~1150 cm^{-1} and a sharper band at ~975 cm^{-1}. Peaks at these positions are consistent with IR band positions for schwertmannite;[42] they are indicative of the outer-sphere coordination of SO_4^{2-}.[42−44] (samples were washed with deionized water, under strict anoxic conditions, prior to analysis) and are not due to the presence of residual surface-adsorbed SO_4^{2-}. These results are consistent with the crystal structure of schwertmannite in which SO_4^{2-} ions reside as counterions in the internal channels of the crystal structure.[43] The other bands at 780−890 cm^{-1} (spectrum at pH 4.5) correspond to structural Fe−OH groups (δOH) in the lattice of Fe phases.[45]

The solution species in the reaction were modeled with PHREEQC[46,47] (WATEQ4F thermodynamic database) using

(40) Bernal, J. D.; Dasgupta, D. R.; Mackay, A. L. The oxides and hydroxides of iron and their structural inter-relationships. *Clay Miner. Bull.* **1959**, *4*, 15−30.

(41) Davidson, L. E.; Shaw, S.; Benning, L. G. The kinetics and mechanisms of schwertmannite transformation to goethite and hematite under alkaline conditions. *Am. Mineral.* **2008**, *93*, 1326−1337.

(42) Peak, D.; Ford, R. G.; Sparks, D. L. An in Situ ATR-FTIR Investigation of Sulfate Bonding Mechanisms on Goethite. *J. Colloid Interface Sci.* **1999**, *218*, 289−299.

(43) Bigham, J. M.; Schwertmann, U.; Carlson, L.; Murad, E. A poorly crystallized oxyhydroxysulfate of iron formed by bacterial oxidation of Fe(II) in acid mine waters. *Geochim. Cosmochim. Acta* **1990**, *54*, 2743−2758.

(44) Nakamoto, K. *Infrared and Raman Spectra of Inorganic and Coordination Compounds*, 6th ed.; Wiley: Hoboken, NJ, 2009; Part A.

(45) Farmer, V. C. *Infrared Spectra of Minerals*; Mineralogical Society: London, 1977.

(46) Parkhurst, D. L.; Appelo, C. A. J. *User's Guide to PHREEQC (Version 2): A Computer Program for Speciation, Batch-Reaction, One-Dimensional Transport and Inverse Geochemical Calculations*. U.S. Geological Survey: Denver, CO, 1999.

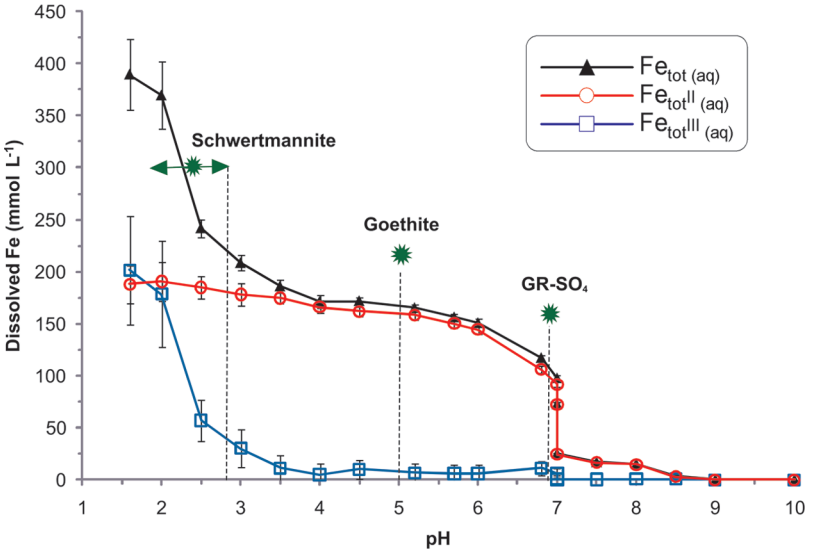

Figure 5. Concentrations of $Fe^{II}_{tot}(aq)$, $Fe^{III}_{tot}(aq)$, and $Fe_{tot}(aq)$ measured using the Ferrozine method from an offline experiment carried out in an equivalent manner to the online $R_{1.28}$ experiment. The symbols represent experimental data points that are connected by solid lines for ease of viewing. The pH at which schwertmannite, goethite, and GR-SO_4 started to form are marked with a star (*).

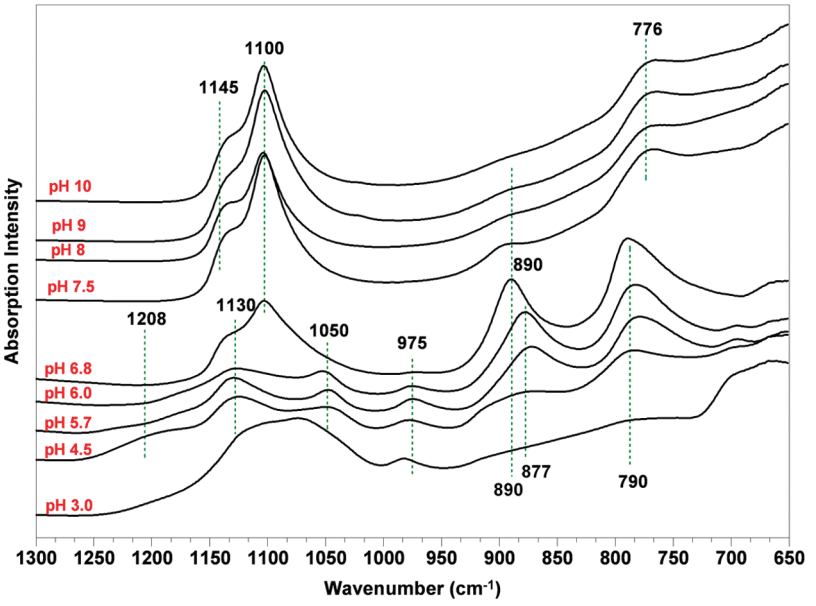

Figure 6. ATR-FTIR spectra of solid phases formed during the synthesis of GR-SO_4 over a range of pH from an offline experiment carried out in an equivalent manner to the online $R_{2.0}$ experiment.

the data obtained from the ferrozine analyses from an off-line experiment conducted in the same manner as the $R_{1.28}$ experiment. The modeling (Figure 7a) revealed that at the low pH (< 3.5) and high SO_4^{2-} concentration in the solution (434 mmol L^{-1}) the predominant Fe^{III} species in solution were $FeSO_4^{+}(aq)$ and $Fe(SO_4)_2^{-}(aq)$ whereas the concentration of $Fe^{3+}(aq)$ was negligible. These results suggest that the formation of schwertmannite occurred via the hydrolysis and polymerization of the aqueous ferric and ferric sulfate complexes and that the sulfate ions complexed to the iron in solution became incorporated into the solid structure once precipitated.

The equation for the formation of schwertmannite from solution has been shown to be[48]

$$8Fe^{3+}(aq) + ySO_4^{2-}(aq) + \frac{24-2y+x}{2}H_2O(l) \leftrightarrow Fe_8O_8(OH)_x(SO_4)_y(s) + (24-2y)H^+(aq) \quad (2)$$

where $8 - x = 2y$ and $1.0 \le y \le 1.75$.

At these high iron and sulfate concentrations, it is reasonable to assume the highest value for $y = 1.75$, and thus the overall reaction leading to the precipitation of schwertmannite can be

(47) Ball, J. W.; Nordstrom, D. K. *User's manual for WATEQ4F, with Revised Thermodynamic Database and Test Cases for Calculating Speciation of Major, Trace and Redox Elements in Natural Waters*; Open-File Report 91-183; U.S. Geological Survey: Denver, CO, 1991.

(48) Bigham, J. M.; Schwertmann, U.; Traina, S. J.; Winland, R. L.; Wolf, M. Schwertmannite and the chemical modeling of iron in acid sulfate waters. *Geochim. Cosmochim. Acta* **1996**, *60*, 2111−2121.

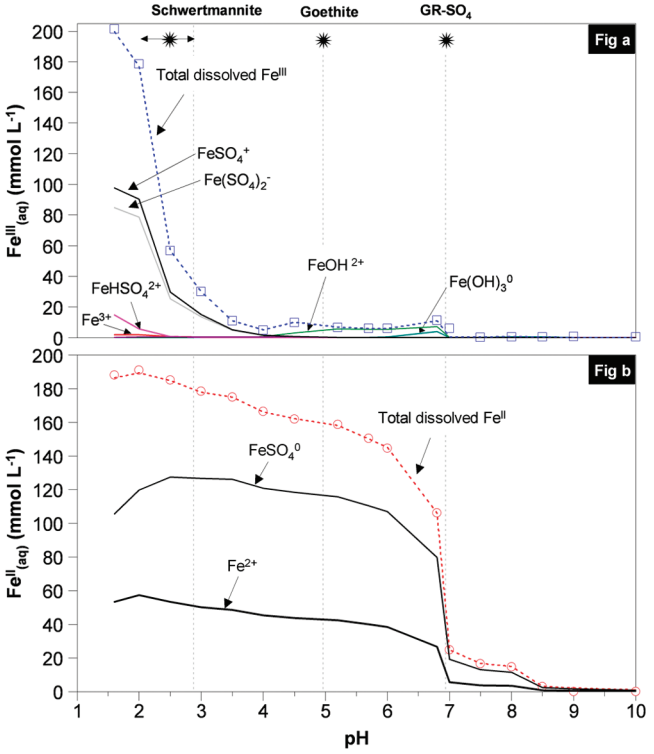

Figure 7. Distribution of dissolved (a) Fe^{II} and (b) Fe^{III} species as a function of pH simulated using PHREEQC. The open symbols represent experimental data for $Fe^{II}{}_{tot}(aq)$ and $Fe^{III}{}_{tot}(aq)$. Solid lines represent the concentration of free and complexed Fe^{II} and Fe^{III} species in solution obtained from PHREEQC simulation.

written as

$$8Fe^{3+}(aq) + 1.75SO_4{}^{2-}(aq) + 12.5H_2O(l) \leftrightarrow Fe_8O_8(OH)_{4.5}(SO_4)_{1.75}(s) + 20.5H^+(aq) \quad (3)$$

The data presented in Figure 5 shows that a significant reduction in $Fe^{III}{}_{tot}$ (aq) concentration occurs at pH 2.5−2.8 with virtually no dissolved Fe^{III} present at pH > 3.5; therefore, the complete reaction in eq 3 requires 199.9 mmol of OH^- to precipitate all of the Fe^{III} in the system as schwertmannite. As shown in Figure 3a, the addition of ~200 mmol of OH^- raised the pH to ~3.6, which coincides with the complete removal (>98%) of all Fe^{III} from solution (Figure 5) and suggests that all OH^- added to the system in this pH range was consumed during the precipitation of schwertmannite. The results from this study suggest a stability field of schwertmannite in the pH range of 2.8−5.0 and the beginning of the transformation to goethite above pH 5. This stability field is similar to that reported in acid mine drainage environments where schwertmannite has been shown to be stable in the pH range of 2.5−4.5[43,49,50] in waters containing between 10.41 and 31.23 mmol of $SO_4{}^{2-}$ L^{-1}. The slight difference in the upper stability limit is likely due to the relatively fast pH increase during the coprecipitation experiments, which may not have given sufficient time for the transformation to goethite to be initiated between pH 4.5 and 5.0.

3.2. Schwertmannite-to-Goethite Transformation (pH 5−7). Above pH ~5, the time-resolved WAXS data (Figures 2 and 3c) show the formation of a peak centered at 13.7° 2θ (d = 4.18 Å) that corresponds to the goethite (101) diffraction peak, and this coincides with the disappearance of the schwertmannite (212) peak (Figure 2). Ex situ X-ray diffraction data from a sample collected at pH 5.7 from an equivalent experiment (Figure 4b) show only peaks for goethite, suggesting a complete transformation of schwertmannite into goethite as the solution pH approaches 6.0. These results are in agreement with WAXS data in Figure 3c that suggest that goethite reaches its maximum intensity at pH ~6.0. WAXS data from the $R_{2.0}$ experiment show a similar trend, with goethite starting to form at pH 5.75 and reaching its maximum intensity at pH 6.9 (Figure S3b).

The ATR-FTIR data (Figure 6) for samples collected at pH 5.7 and 6.0 ($R_{2.0}$) show clear bands at 877 and ~790 cm^{-1}, which are the most frequently used mid-infrared vibrations for indentifying structural Fe−OH in goethite.[42,51] The bands at 1130, 1050, and 975 cm^{-1} were assigned to $SO_4{}^{2-}$ groups sorbed specifically or nonspecifically to the goethite surface, in line with the study of Peak et al.[42]

SEM images of samples collected at pH 6.2 ($R_{1.28}$, Figure 8a) show that the goethite particles are < 50 nm in size with a slightly elongated shape. This particle size is consistent with the particles being "nanogoethite", which is thought to be one of the dominant reactive iron phases in many natural environments (e.g., marine sediments).[52] The nanosize of goethite particles formed is also responsible for the broad diffraction peaks observed in the WAXS and offline XRD data (Figures 2 and 4).

3.2.1. Mechanism of Goethite Formation. A number of studies have shown that synthetic schwertmannite is thermodynamically unstable with respect to goethite in the pH range of 3−6 and that above pH 4 schwertmannite transforms to goethite and releases the structurally bound sulfate from its lattice.[48,53] Calculations based on data by Jönsson et al.[54] indicated that the transformation of natural schwertmannite to goethite at pH 6 under oxic conditions was incomplete even after 514 days. In the current study, schwertmannite transformed to goethite in ~1.0 h over a small pH range (>4.5 and <~6.0), which suggests that this transformation is not solely dependent on pH change but that other factors must be considered. Recently, Burton et al.[53,55] showed that the presence of adsorbed Fe^{2+}(aq) catalyzed the transformation of schwertmannite to goethite at a rate of 22.7% h^{-1} at pH 6.5, which is several orders of magnitude greater than the values reported in the absence of Fe^{2+}(aq). Burton et al.[55] suggested that the adsorption of Fe^{2+} ions onto schwertmannite may be significant at pH > 5. The Fe data (Figure 5) support these findings because they show a steady decrease in $Fe^{II}{}_{tot}$(aq) with increasing pH beyond ~4.5, which is likely due to adsorption onto the suspended ferric oxyhydroxide particles. The speciation analysis (Figure 7b) of the dissolved iron in solution from experiment $R_{1.28}$ indicates that at pH 4.0 ~50% of the dissolved Fe^{II} is present as free Fe^{2+} ions, with the remaining iron being

(49) Carlson, L.; Bigham, J. M.; Schwertmann, U.; Kyek, A.; Wagner, F. Scavenging of As from acid mine drainage by schwertmannite and ferrihydrite: A comparison with synthetic analogues. *Environ. Sci. Technol.* **2002**, *36*, 1712−1719.

(50) Cravotta, C. A.; Brady, K. B. C.; Rose, A. W.; Dounds, J. B. *Frequency distribution of the pH of coal-mine drainage in Pennsylvania*; Morganwalp, D. W., Buxton, H., Eds.; U.S. Geological Survey Toxic Substances Hydrology Program. USGS Water Resources Investigation Report 99 -4018A, pp 313−324.

(51) Cornell, R. M.; Schwertmann, U. *The Iron Oxides: Structure, Properties, Reactions, Occurrences and Uses*; Wiley-VCH: Weinheim, Germany, 2003.

(52) van der Zee, C.; Roberts, D. R.; Rancourt, D. G.; Slomp, C. P. Nanogoethite is the dominant reactive oxyhydroxide phase in lake and marine sediments. *Geology* **2003**, *31*, 993−996.

(53) Burton, E. D.; Bush, R. T.; Sullivan, L. A.; Mitchell, D. R. G., Schwertmannite transformation to goethite via the Fe(II) pathway: Reaction rates and implications for iron-sulfide formation. *Geochim. Cosmochim. Acta* **2008**, *72*, (18), 4551−4564.

(54) Jönsson, J.; Persson, P.; Sjöberg, S.; Lövgren, L. Schwertmannite precipitated from acid mine drainage: phase transformation, sulphate release and surface properties. *Appl. Geochem.* **2005**, *20*, 179−191.

(55) Burton, E. D.; Bush, R. T.; Sullivan, L. A.; Mitchell, D. R. G. Reductive transformation of iron and sulfur in schwertmannite-rich accumulations associated with acidified coastal lowlands. *Geochim. Cosmochim. Acta* **2007**, *71*, 4456−4473.

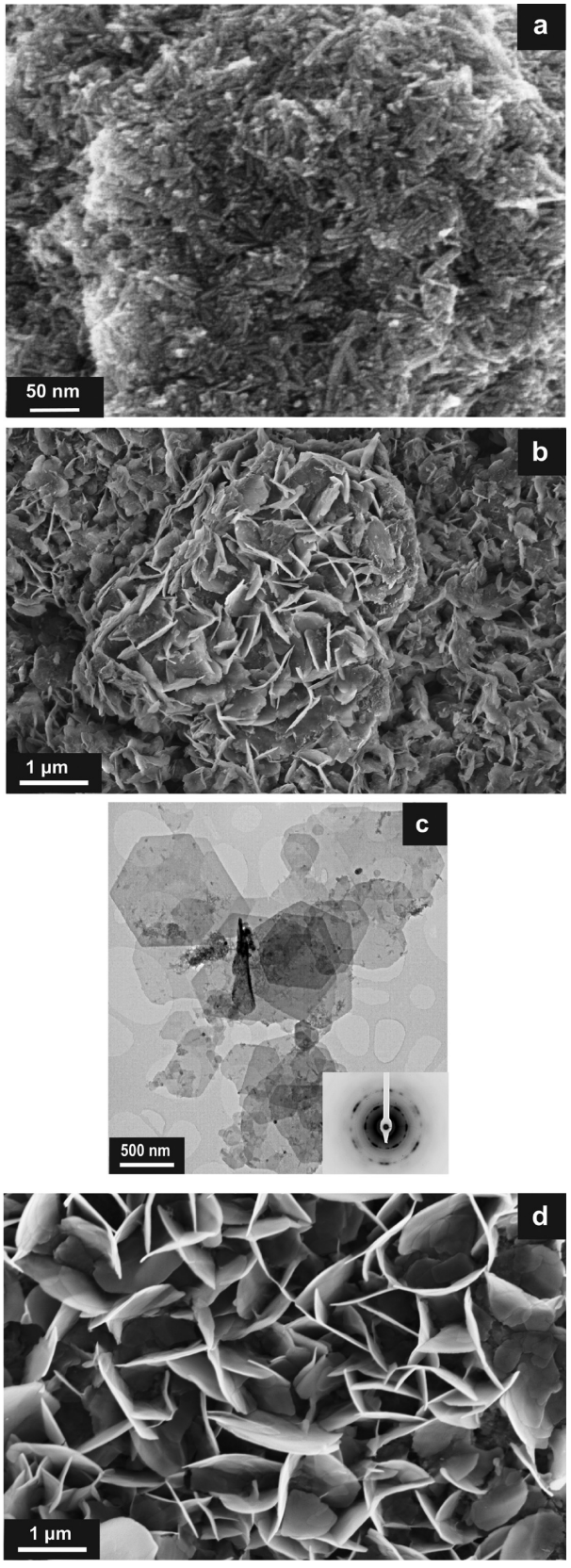

Figure 8. Photomicrographs of precipitates formed during the synthesis of GR-SO_4 in the $R_{1.28}$ experiment: (a) SEM image of goethite (< 50 nm) formed at pH 5.7. (b) SEM image of GR-SO_4 and the goethite sample formed at pH 7 (t = 2.2 h). (c) TEM image of hexagonal GR-SO_4 particles at pH 7.5. The inset is an SAED pattern of GR-SO_4 showing the distinctive hexagonal diffraction pattern of GR. (d) SEM image of GR-SO_4 particles formed at pH 8.5.

present as the $FeSO_4^0$(aq) complex. Previous studies have also highlighted the role of Fe^{2+} ions in catalyzing the abiotic transformation of other poorly ordered ferrihydrite ($Fe_2O_3 \cdot H_2O$) to more crystalline phases such as goethite and lepidocrocite (γ-FeOOH).[56−59] We suggest that a similar Fe^{2+}-catalyzed transformation process explains the rapid transformation of schwertmannite to goethite in the current study. This transformation occurs first by the adsorption of Fe^{2+} to the surface of schwertmannite (increasingly significant at pH > 5), which facilitates electron transfer between Fe^{3+} in the solid phase and surface-bound Fe^{2+} ions. This reaction decreases the stability of the schwertmannite crystal and causes a rearrangement of the structure and therefore the transformation of schwertmannite to goethite.[48,60] This reaction can be described as follows:

$$Fe_8O_8(OH)_{4.5}(SO_4)_{1.75}(s) + 3.5OH^-(aq) \xrightarrow{Fe^{2+}_{(aq)}} 8FeOOH(s) + 1.75SO_4^{2-}(aq) \quad (4)$$

According to eq 4, the complete transformation of schwertmannite to goethite requires the addition of 34 mmol of OH^- for the $R_{1.28}$ experiment (i.e., a total of ~234 mmol OH^- up to this point in the reaction), which corresponds to pH ~5.8 as shown in Figure 3b. This is consistent with the time-resolved WAXS data (Figure 3c) that indicate that the goethite diffraction peak reaches its maximum intensity at pH ~6.0. The 0.2 pH difference is likely to be due to the kinetics of goethite formation and that the pH was constantly increased with time, therefore the formation of goethite would finish above pH 5.8.

3.3. Formation of GR-SO_4. The WAXS data (Figure 4c) for the $R_{1.28}$ experiment show that at pH ~6.9 (t = 2.28 h) the goethite (101) diffraction peak begins to decrease in intensity; this decrease coincides with the beginning of the formation and growth of narrow and distinct peaks for GR-SO_4. After ~6 h (pH 7), there is an approximate 40% decline in the goethite integrated peak area and an associated increase in the GR-SO_4 peak area to ~40% of its final maximum intensity (Figure 4c). Only a small drop in the intensity of the goethite peak occurred between t = 5.81 and 8.9 h ($R_{1.28}$), during which time the pH was held constant at 7.0. After this period, the pH was increased to 10 over 4.4 h. During this phase of the reaction, there was a second sharp decline in the intensity of the goethite (101) peak and an associated increase in the intensity of GR-SO_4 peaks (Figures 2 and 3) until GR-SO_4 was the only crystalline product at pH 8.5−10. During the formation of GR-SO_4, the concentration of Fe^{II}_{tot} (aq) (Figure 5) dropped significantly (> pH ~6) until it reached almost zero at pH ~8. This was mirrored by a significant drop in Eh from −245 mV at pH 7 to −340 mV at pH ~8.0 (Figure 3b), a decrease that is primarily due to the increase in pH.

The SEM micrograph of a sample ($R_{1.28}$) collected at pH 7 (Figure 8b) shows an aggregated mixture of nanoparticulate goethite and platelike particles of GR-SO_4. The TEM image of a sample collected at pH 7.5 (Figure 8c) clearly shows that

(56) Hansel, C. M.; Benner, S. G.; Fendorf, S. Competing Fe(II)-induced mineralization pathways of ferrihydrite. *Environ. Sci. Technol.* **2005**, *39*, 7147.
(57) Pedersen, H. D.; Postma, D.; Jakobsen, R.; Larsen, O. Fast transformation of iron oxyhydroxides by the catalytic action of aqueous Fe(II). *Geochim. Cosmochim. Acta* **2005**, *69*, 3967−3977.
(58) Andreeva, D.; Mitov, I.; Tabakova, T.; Mitrov, V.; Andreev, A. Influence of iron (II) on the transformation of ferrihydrite into goethite in acid medium. *Mater. Chem. Phys.* **1995**, *41*, 146−149.
(59) Yee, N.; Shaw, S.; Benning, L. G.; Nguyen, T. H. The rate of ferrihydrite transformation to goethite via the Fe(II) pathway. *Am. Mineral.* **2006**, *91*, 92−96
(60) Regenspurg, S.; Brand, A.; Peiffer, S. Formation and stability of schwertmannite in acidic mining lakes. *Geochim. Cosmochim. Acta* **2004**, *68*, 1185−1197.

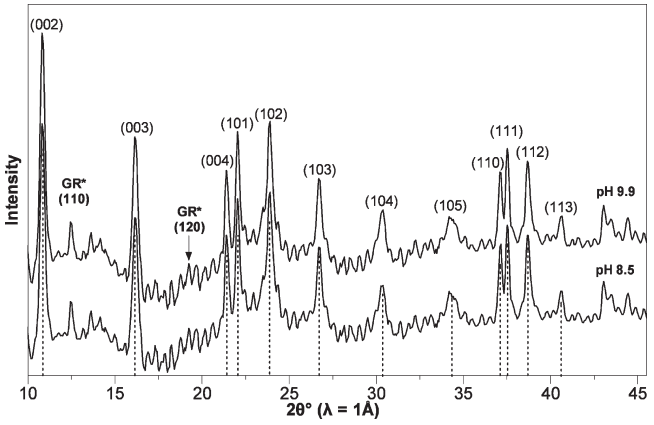

Figure 9. WAXS patterns of $GRSO_4$ collected at pH 8.5 and 9.9 from the online $R_{1.28}$ experiment. Peak positions in the experimental data are compared to those determined for GR-SO_4 (vertical dotted lines) by Simon et al.[3] The GR peak positions match those indexed by Bernal et al.[40] and Simon et al.,[3] except for the peaks labeled GR* that were recently indexed by Christiansen et al.[9]

GR-SO_4 particles exhibit a thin (<20 nm), hexagonal, platelike morphology[27,61] with an average particle size of $<1\ \mu$m. The inset in Figure 8c shows an SAED pattern that displays a hexagonal diffraction pattern indicative of GR. As the pH increased to 8.5, the solids were pure GR-SO_4 with no more goethite present (Figure 8d). These observations are consistent with WAXS diffraction data collected at pH 8.5 and 9.9 in the $R_{1.28}$ experiment (Figure 9) that show that at pH >8.5 the product is purely GR-SO_4 with no goethite peaks.

Although the WAXS data for the $R_{2.0}$ experiment (Figure S3b) show a similar trend to the $R_{1.28}$ experiment (GR-SO_4 formation at pH >6.95 and a simultaneous decrease in the intensity of the goethite diffraction peak), the final product in the $R_{2.0}$ experiment (even at pH 10) was not pure GR-SO_4 but still contained small amounts of goethite. The ATR-FTIR data ($R_{2.0}$) at pH 7.5 and above (Figure 6) show that the two bands at 1130 and 1050 cm^{-1} are replaced by a more intense, narrow band at 1100 cm^{-1} with a small shoulder around 1145 cm^{-1}. These bands can be attributed to SO_4^{2-} within the interlayer of the GR structure (split v_3 mode),[61,62] indicating that the SO_4^{2-} ions that were adsorbed to the surface of goethite became intercalated within the newly forming GR-SO_4 structure. This is in accordance with literature data[62] that revealed that such splitting is indicative of sulfate intercalation within the LDH structure and nonsymmetric interactions with the $Fe(OH)_6$ octahedra. Finally, the broad band at 776 cm^{-1} attributable to lattice Fe−OH[62] in the GR-SO_4 structure is at a substantially lower wavenumber than the structural Fe−OH peak for goethite (~790 cm^{-1}), again supporting the WAXS data that showed GR-SO_4 to be the dominant end product in the $R_{2.0}$ experiment.

Changes in the unit cell parameters of GR-SO_4 during its formation and crystallization are shown in Figure 10. The average unit cell parameters of GR-SO_4 in the $R_{1.28}$ experiment were a = 3.19 Å and c = 11.07 Å, which are consistent with previously published parameters for GR-SO_4.[2] There is virtually no change in the a-axis dimension during crystallization, indicating that there is no rearrangement or ordering within the $a-b$ plane during its formation. However, the c-axis length decreases slightly (~0.005 Å) during crystallization, which may indicate the ordering of interlayer water and/or sulfate molecules as the particles grow. The crystallite sizes calculated from the fwhm of the (003) peak using the Scherrer analysis indicate a thickness of the GR-SO_4 platelets of ~70 Å in the pH range of 7 to 7.5 and an increase to ~150 Å by pH 8.5 (Figure 10). The average particle diameters ($a-b$ crystallographic plane) of GR-SO_4 determined from the SEM images were 430 and 709 nm at pH 7.0 and 8.5, respectively. The estimated average thickness of the GR-SO_4 hexagonal plates at pH 9.0, determined from the SEM micrographs, was ~16 nm, excluding ~3 nm of Pt coating on both sides of the GR plate, which is comparable to the thickness obtained using Scherrer analysis (i.e., 15 nm). These results indicate that during the formation of GR, particle growth was predominantly in the $a-b$ crystallographic plane with a significantly slower growth rate along the c axis.

3.3.1. Mechanisms of GR Formation. The normalized peak area (α) versus time of goethite and GR-SO_4 for the $R_{1.28}$ experiment (Figure 3c) shows that after 5.0 h at pH 7 the amount of goethite is reduced by ~40% and is not detectable by pH 8.5. This reduction in goethite is mirrored by an equivalent increase in GR-SO_4 formed. These results suggest the complete transformation of goethite to GR-SO_4 and that all initial Fe^{II} and Fe^{III} were consumed during the formation of GR-SO_4 at pH >8.5. This is supported by the electron microscopy image data that indicate that only goethite and GR-SO_4 are present above pH 7 and that GR-SO_4 is the final and only material formed at pH >8.5. Thus, the overall reaction leading to the formation of GR-SO_4 from initial Fe^{II}/Fe^{III} = 1.28:1 is given in eq 5.

$$3.13Fe^{3+}(aq) + SO_4^{2-}(aq) + 4Fe^{2+}(aq) + 15.39OH^-(aq) \leftrightarrow Fe^{II}_4Fe^{III}_{3.13}(OH)_{15.39}SO_4(s) \quad (5)$$

$$2Fe^{3+}(aq) + SO_4^{2-}(aq) + 4Fe^{2+}(aq) + 12OH^-(aq) \leftrightarrow Fe^{II}_4Fe^{III}_2(OH)_{12}SO_4(s) \quad (6)$$

$$3.13Fe^{3+}(aq) + SO_4^{2-}(aq) + 4Fe^{2+}(aq) + 15.39OH^-(aq) \leftrightarrow Fe^{II}_4Fe^{III}_2(OH)_{12}SO_4(s) + 1.13FeOOH(s) + 1.13H_2O(l) \quad (7)$$

For the reaction in eq 5 to reach completion, a total of 385 mmol of OH^- must be added to the system in order to form GR-SO_4 with no residual goethite. The experimental data presented in Figure 3b show that in the $R_{1.28}$ experiment ~390 mmol of OH^- was added to reach pH 8.5, which is in good agreement with the above calculations. In the $R_{2.0}$ experiment, GR-SO_4 reaches its maximum at pH 8.0, at which ~312 mmol of OH^- was consumed (Figure S3a). This is also in good agreement with calculations from eq 6 that indicates that the reaction should consume 300 mmol of OH^-. The small differences between the calculated and experimental values of consumed OH^- are likely to be due to changes in sulfate speciation with increasing pH (i.e., $H_2SO_4 \rightleftharpoons HSO_4^- \rightleftharpoons SO_4^{2-}$), which would consume OH^-. These chemical data suggest that for the $R_{1.28}$ experiment the structural Fe^{II}/Fe^{III} ratio in the GR-SO_4 that is formed is 1.28, which supports the results from the WAXS and electron microscopy images. For the $R_{1.28}$ experiment, if GR-SO_4 was formed with a Fe^{II}/Fe^{III} ratio of 2.0, then this necessitated the presence of ~36% of the original Fe^{III} as FeOOH at the end of the reaction (eq 7). The data presented in this study suggest that all of the Fe^{II} ions from

(61) Génin, J. M. R. Fe(II-III) hydroxysalt green rusts; from corrosion to mineralogy and abiotic to biotic reactions by Mössbauer spectroscopy. *Hyperfine Interact.* **2004**, *156−157*, 471−485.

(62) Peulon, S.; Legrand, L.; Antony, H.; Chaussé, A. Electrochemical deposition of thin films of green rusts 1 and 2 on inert gold substrate. *Electrochem. Commun.* **2003**, *5*, 208−213.

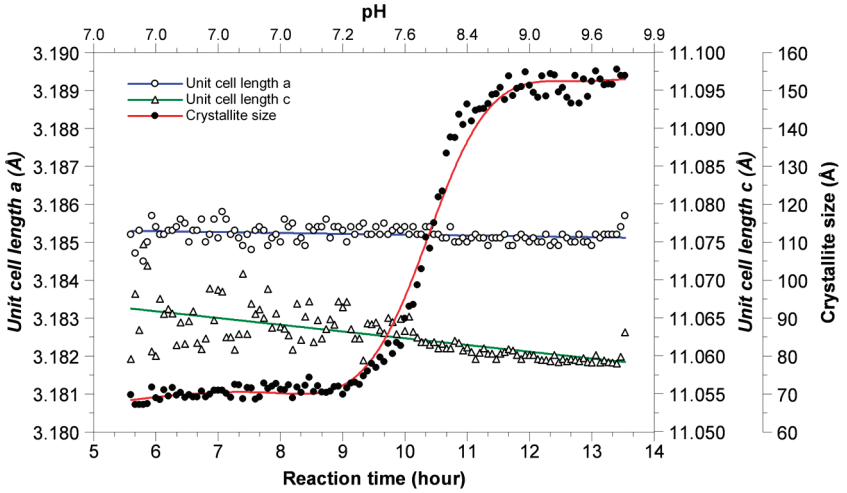

Figure 10. Crystallite size and unit cell dimensions of GR-SO_4 vs time and pH in the $R_{1.28}$ experiment. Solid lines on the unit cell dimensions are linear regression fits to the experimental data. The solid line on the crystallite size data is a guide to the eye.

solution were consumed during the formation of GR-SO_4 and that any α-FeOOH transformed gradually with increasing pH. Also, note that there was no evidence of $Fe(OH)_2$ (white rust) or Fe_3O_4 (magnetite) formation at any stage during the reaction.

The formation of GR-SO_4 with an Fe^{II}/Fe^{III} ratio of <2 is in agreement with the study of Mazeina et al.,[63] who synthesized GR-SO_4 by coprecipitation and oxidation methods at Fe^{II}/Fe^{III} ratios of 0.5, 1.21, and 1.34. In addition, Génin et al.[64] reported structural Fe^{II}/Fe^{III} ratios of ~0.5 − 3.0 in the mineral fougerite (IMA 2003-057), which is thought to belong to the GR family of compounds. However, Géhin et al.[27] prepared GR-SO_4 by coprecipitation using initial Fe^{II}/Fe^{III} ratios of 0.3−3.0 and indicated that the structural Fe^{II}/Fe^{III} of the GR formed was 2 in all cases, although no direct analysis of GR-SO_4 samples synthesized at Fe^{II}/Fe^{III} ratios <2.0 were presented. Conversely, Refait et al.[1] using Mössbauer analysis on an aged solid phase produced by coprecipitation using an initial Fe^{II}/Fe^{III} ratio of 1 showed that at pH 8.1 the product was a mixture of GR-SO_4 ($Fe^{II}/Fe^{III} = 2$), goethite, and magnetite. These authors suggested that the formation of GR-SO_4 is independent of the initial Fe^{II}/Fe^{III} ratio in solution. In the present study, data from the $R_{1.28}$ experiment indicate that GR-SO_4 was not fully formed until pH 8.5 and any GR-SO_4 formed at a lower pH may have $Fe^{II}/Fe^{III} \neq 2$; therefore, we suggest that the composition of GR may be partially controlled by the pH of the solution. As the pH is increased, goethite reacts to form GR. However, the final composition is not achieved until GR has fully formed above pH 8.2−8.5, and any GR samples collected below this pH may have a higher Fe^{II}/Fe^{III} ratio. This is supported by the solution analyses that show that the rate at which Fe^{II}_{tot} (aq) declines is faster than the rate of goethite consumption (Figures 3 and 5) because most of the dissolved Fe^{II} is consumed before all of the goethite is depleted. Therefore, any GR-SO_4 formed before the GR formation is complete may have a higher Fe^{II}/Fe^{III} ratio than the stoichiometry of the initial solution. The changing Fe^{II}/Fe^{III} ratio during formation would be facilitated by electron-transfer processes within the octahedral layers. These results illustrate the advantages of in situ characterization throughout the GR formation process without the preparations required for ex situ analyses (e.g., washing, freeze drying, and aging), which could cause artifacts due to recrystallization or oxidation (e.g., changes in the Fe^{II}/Fe^{III} ratio or oxidation to form goethite/magnetite).

Results from the $R_{2.0}$ experiment show that although GR is the dominant reaction product there is some goethite present at the end of the experiment (pH 10, Figure S3), and thus the Fe^{II}/Fe^{III} ratio of the GR-SO_4 formed was >2. However, because of the dominance of GR-SO_4 diffraction peaks in the WAXS data relative to those for goethite, it is likely that the GR Fe^{II}/Fe^{III} ratio is close to 2. These results seem to be inconsistent with the $R_{1.28}$ experiment and with previous studies[2] that suggest an ideal stoichiometry for GR-SO_4 of 2 and GR-SO_4 as the only end product. The reason for the presence of goethite at the end of the $R_{2.0}$ experiment but not the $R_{1.28}$ experiment may be due to the stability of the goethite formed during the second stage of the reaction (pH 5−6.9). In the $R_{2.0}$ experiment, the Fe^{II}/Fe^{III} ratio in the system is significantly higher than in the $R_{1.28}$ experiment (36% higher), which could lead to an increased rate of goethite crystallization.[59] Also, in the $R_{2.0}$ experiment the pH was increased to 7 over 2.9 h whereas in the $R_{1.28}$ experiment it was 2.2 h. Both of these factors may have led to an increase in the crystallinity and/or particle size of the goethite formed during the second stage of the reaction. This more crystalline goethite may take longer to transform to GR above pH 6.9, but given long enough, it is likely that the small amount of residual goethite may fully transform to GR with time. If goethite crystallization is the controlling factor in the final GR composition, its presence highlights the potential influence of the precursor phases on the stoichiometry of the GR formed during the coprecipitation synthesis methods.

Data from the solution analyses (Figure 5) indicate that there is a decrease in the concentration of Fe^{II}_{tot}(aq) that coincides with the formation of GR-SO_4 at pH ~7 (Figure 3c). This decrease in Fe^{II}_{tot}(aq) is due to Fe^{2+} hydrolysis and its incorporation into solid GR particles, although the mechanism by which this occurs is unclear. Below pH 7, Fe^{2+} does not hydrolyze but will adsorb to the surface of FeOOH.[65] This adsorbed Fe^{2+} has been shown to ion exchange rapidly (hours) and completely with the structural Fe^{3+} in goethite via electron-transfer reactions, but at low pH

(63) Mazeina, L.; Navrotsky, A.; Dyar, D. Enthalpy of formation of sulfate green rusts. *Geochim. Cosmochim. Acta* **2008**, *72*, 1143−1153.
(64) Génin, J. M. R.; Bourrie, G.; Trolard, F.; Abdelmoula, M.; Jaffrezic, A.; Refait, P.; Maitre, V.; Humbert, B.; Herbillon, A. Thermodynamic equilibria in aqueous suspensions of synthetic and natural Fe(II)-Fe(III) green rusts: occurrences of the mineral in hydromorphic soils. *Environ. Sci. Technol.* **1998**, *32*, 1058−1068.
(65) Hiemstra, T.; van Riemsdijk, W. H. Adsorption and surface oxidation of Fe(II) on metal (hydr)oxides. *Geochim. Cosmochim. Acta* **2007**, *71*, 5913−5933.

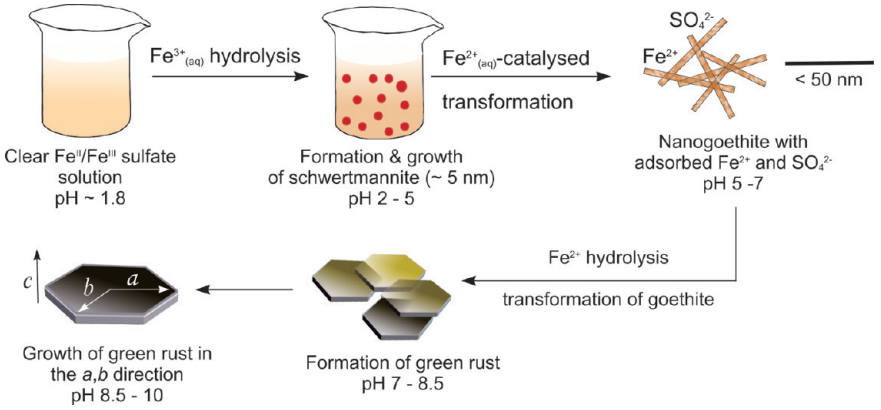

Figure 11. Schematic summary of the stages involved in the formation of GR-SO_4 and its precursors.

(< 7), the Fe^{2+} formed is released back into solution.[66] As the pH increases, the electron-transfer reaction between Fe^{2+} and Fe^{3+} will continue to occur, but as the solubility of Fe^{2+} decreases, it will no longer be released into solution but instead will become incorporated into the iron oxyhydroxide structure. We propose that this process occurs above pH 7 and leads to the formation of mixed Fe^{II}/Fe^{III} brucite octahedral sheets, which are stabilized in the solution by adsorbed sulfate ions. These sheets are the primary structural units of GR-SO_4 that will form and grow as Fe^{2+} hydrolysis continues to occur (Figure 11). GR-SO_4 growth will be predominantly in the $a-b$ crystallographic plane to form platelike GR-SO_4 particle morphology,[28] which is supported by particle size analysis during the crystallization reaction from the WAXS (Figure 10) and SEM (Figure 8) data evaluations. Ruby et al.[28] indicated a similar mechanism of GR-SO_4 formation but suggested that brucite-like Fe^{II} clusters form in solution and are then attracted to the surface of FeOOH particles and trap a layer of sulfate ions between the FeOOH surface and the Fe^{II} sheet. The data from this study do not supports this hypothesis because it is likely that the Fe^{II} ions hydrolyze on the surface of the FeOOH (i.e., goethite) particles and direct bonding of the Fe^{2+} ion onto the surface facilitates the electron-transfer process that is key to initiating the recrystallization process.[66] It is also unlikely that large clusters of Fe^{II} species will form in solution because most of the Fe^{II} is associated with the solid phase by pH 7. The pathway for the formation and growth of GR-SO_4 is summarized in Figure 11.

4. Conclusions

The potentiometric titration of mixed Fe^{II}/Fe^{III} sulfate solutions under anoxic conditions with initial Fe^{II}/Fe^{III} ratios of 1.28 and 2.0 showed that the composition of GR-SO_4 is dependent on the initial Fe^{II}/Fe^{III} ratio and the final pH of the synthesis. The in situ and ex situ XRD data and ATR-FTIR data provided evidence of the formation of schwertmannite at low pH and its transformation to goethite due to the catalytic effect of surface-adsorbed Fe^{2+} ions. The proposed mechanism for the formation of GR-SO_4 is via the hydrolysis of surface-adsorbed Fe^{2+} coupled with electron-transfer processes at the solid/solution interface, which leads to the transformation of goethite to GR-SO_4.

This mechanistic information provides key parameters that can tailor the production of GR to industrial applications and its formation and stability to the natural environment. First, GR-SO_4 can be formed at variable Fe^{II}/Fe^{III} ratios by fixing the ratio of the starting solution and titrating the solution to pH > 8.5 to ensure full transformation to GR. Second, the stability of GR-SO_4 covers a wide range of pH; therefore, GR-SO_4 may be quite prevalent in natural anoxic systems such as hydromorphic soils.

Acknowledgment. We gratefully acknowledge the Natural Environment Research Council (NERC, grant no. NE/D014026/1) for funding this research. We also thank the CCLRC for the provision of facilities at the Daresbury Synchrotron Radiation Laboratory (SRS grant no. 48163) and the Diamond Light Source (SRS grant no. SM883). Moreover, we thank Dr. Chris Martin (station MPW6.2) at the SRS Daresbury Laboratory and Dr. Marc Malfois and Dr. Claire Pizzey at the Diamond Light Source (station I22) for their excellent support and help in undertaking the WAXS experiments. Thanks are also extended to the technical support staff at the Leeds Electron Microscopy and Spectroscopy (LEMAS) centre for assistance during the SEM/TEM image collection and analysis.

Supporting Information Available: A short movie of GR-SO_4 formation in a reaction vessel. Stacked plot of in situ WAXS data from the $R_{2.0}$ experiment. *Eh*−pH versus time profile for the $R_{2.0}$ experiment. Comparison between *Eh* versus pH and titration curves from the $R_{2.0}$ and $R_{1.28}$ experiments. This material is available free of charge via the Internet at http://pubs.acs.org.

(66) Handler, R. M.; Beard, B. L.; Johnson, C. M.; Scherer, M. M. Atom exchange between aqueous Fe(II) and goethite: an Fe isotope tracer study. *Environ. Sci. Technol.* **2009**, *43*, 1102−1107.